

Growth and structure of tin dioxide thin films obtained by an improved spray pyrohydrolysis technique

M. Miki-Yoshida and E. Andrade.

Abstract

Undoped and doped tin dioxide thin films have been prepared by an improved method of spray pyrohydrolytic decomposition of $\text{SnCl}_4 \cdot 5\text{H}_2\text{O}$ onto a glass substrate. We show that, with this overhead hot-plate and counter flux spray, the gravitational force plays an important role in distinguishing droplets with a radius greater than $26 \mu\text{m}$. X-ray diffraction spectra show that the structure is polycrystalline, with a grain size in the range 24-100 nm and a preferred orientation that is thickness dependent. It is shown by observations of the film microstructure by transmission electron microscopy that there is first an amorphous layer with embedded crystallites over which many crystals grow. This microstructure suggests that the films start to grow in an amorphous manner, then film growth continues with the nucleation of many small crystallites and finally some of them grow until a closely packed microstructure of crystallites is formed. Scanning electron microscopy of film surfaces indicates that surface roughness could be responsible for the large decrease in optical transmission of some films. Rutherford backscattering spectroscopy shows that film stoichiometry is close to the SnO_2 phase and no significant chlorine contamination is present in the films.

Introduction

Tin dioxide (SnO_2) in its stoichiometric form is an insulator, but in practice the non-stoichiometric form is always encountered, and therefore it acts as an n-type

semiconductor with a wide band gap. Prepared adequately, it has some very important properties, such as high electrical conductivity, high transparency in the visible region, high reflectivity in the IR region, good adhesion to the substrate, and very good chemical stability and mechanical resistance. The fields of application are several, such as solar energy, optoelectronics, metallurgical coatings, gas sensors etc. These films are prepared by several methods, e.g. chemical vapour deposition (CVD) [1], spray pyrohydrolysis or spray pyrolysis [2], corona spray pyrolysis [3], reactive sputtering [4] and reactive evaporation [5]. Among these, spray pyrohydrolysis, *i.e.* the thermal decomposition and hydrolysis of hydrated SnCl_4 solution sprayed onto a hot substrate, is a simple and inexpensive process for large-area substrate application; the only limitation is the low deposition efficiency, defined as the ratio of atoms effectively deposited to those supplied. Recently, the deposition efficiency has been improved by the addition of a corona discharge to control the transport of aerosol droplets towards the substrate; and efficiency as great as 80% is reported [3].

Films obtained by the method used here have optical, electrical, compositional and structural properties similar to those reported previously [6-9]. The optical transmittance in the visible region varied between 67 and 90%. Electrical resistivities were found between 2.6×10^{-2} and $3.2 \times 10^{-3} \Omega \text{ cm}$ for undoped films, and between 1.8×10^{-3} and $1.3 \times 10^{-4} \Omega \text{ cm}$ for F-doped films. A figure of merit defined by Haacke [10] was in the range $1.1 \times 10^{-4} - 2.7 \times 10^{-3}$. The film uniformity was good; no difference in coloured rings were observed in samples with a surface area as large as 70 mm x 70 mm. the same system has been used to obtain other materials such as ZnO, Cu_2O and $\text{NiO}(\text{OH})_x$.

In this paper, we report a new spray and deposition chamber that improves the selectivity of the droplets that arrive close to the substrate. Owing to the geometry of the chamber and to the gravitational force, which is proportional to r^3 (r is the droplet radius), the larger droplets cannot be transported by the carrier gas and therefore return to the spray chamber.

The grain size and preferential growth direction were studied by X-ray diffraction. The microstructure of the films was determined from transmission electron microscopy (TEM) analysis, and important insight into the growth of the films was obtained. We have compared the surface grain size measured in scanning electron micrographs with that calculated from X-ray spectra and that obtained from transmission electron micrographs. The surface roughness was studied by scanning electron microscopy (SEM) and correlated with the optical transmittance of the films.

The stoichiometry and film thickness were analysed by Rutherford backscattering spectrometry (RBS). The degree of inclusion of probable contaminants such as Cl or Na was also determined by this analysis.

Experimental details

Deposition equipment and sample preparation:

Figure 1 shows a schematic representation of the deposition system; the abbreviations used in this figure for the different parts of the equipment will be used later.

A counterflux spraying chamber SCH and overhead deposition chamber DCH were empirically developed to obtain a mist of the solution with small droplets and a

uniform distribution, two necessary conditions for good quality thin films prepared by spray pyrohydrolysis. We have tried different system configurations, such as overhead and bottom oven, and different nozzle geometries and have also optimized parameters such as the distance from the nozzle aperture to the substrate and from the spray to the bottom of the spraying chamber. The system evaluation was performed by optical microscopy to estimate the droplet radius and by means of an optical mist flowmeter, developed in our laboratory, to compare qualitatively the different spraying conditions.

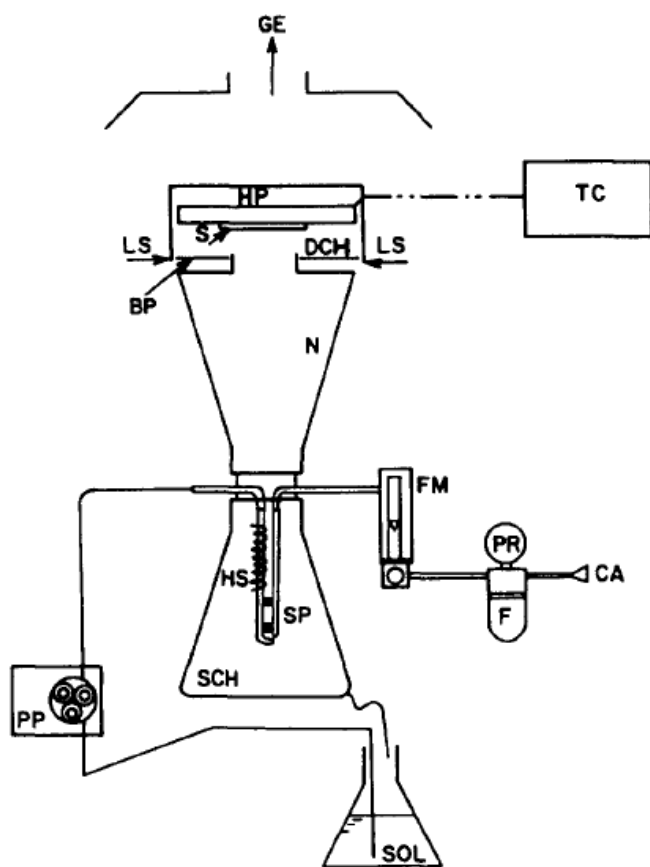


Fig. 1. Schematic representation of the deposition apparatus (from top to bottom): GE, gas evacuation; HP, overhead hot-plate; TC, temperature controller; S, substrate; LS, lateral screening; DCH, deposition chamber; BP, bottom plate; N, nozzle; FM, flowmeter; PR, pressure regulator; HS, heating stage; CA, compressed air; SP, glass spray; F, carrier gas filter; SCH, counterflux spraying chamber; PP, peristaltic pump; SOL, solution of source compound.

A conventional glass-made spray SP was used with a heating stage HS to prevent crystallization of the source compound. The temperature of the solution near the spray was maintained at around 343 K. A peristaltic pump PP for feeding the solution to the spray was utilized. The solution flow was kept in the range 3.3- 80 ml min⁻¹. The source compound was SnCl₄·5H₂O (99.9% purity) dissolved in ethylalcohol SOL; the molar concentration was varied in the range 0.05-0.5 M. The carrier gas was compressed air CA at a typical flux of 250 ml s⁻¹, controlled by a pressure regulator PR and a 5 μm filter F, for preventing contamination of the film due to dust particles or oil. The glass nozzle N has a circular aperture of approximately 8 cm diameter which causes a laminar flow of the mist near the hot substrate. The mist flow rate was in the range 1-2 ml min⁻¹.

During deposition the overhead hot-plate (HP) temperature was controlled to within + 5 °C. The substrate temperature was varied between 523 and 673 K. We also used lateral screening LS to prevent the droplets from being carried out of the coating region. Some ventilation was provided for gas evacuation by setting up the complete system inside a chemical fume hood GE.

The glass substrates S used were microscope slides of size 25 mm × 75 mm × 1 mm and commercial glasses of size 70 mm × 70 mm × 4 mm, which had been previously immersed in concentrated hydrochloric and nitric acid, and then washed with abundant deionized water. They were firmly attached onto the hot-plate.

The deposition time was varied between 4 and 25 min, for several substrate temperatures, in order to evaluate the thickness dependence of physical properties.

In Table 1 the preparation parameters and some physical properties of the tin dioxide films are shown. Other fixed deposition parameters were as follows: solution concentration, 0.3 M; mist flow rate, $2.5 \times 10^{-2} \text{ml s}^{-1}$; air flow rate, 250ml s^{-1} . Film D was doped with F; the dopant source was NH_4F at 0.6 wt.% in solution.

Characterization:

Optical transmission data in the wavelength range 250-900nm were recorded on a Milton Roy 3000 diode array spectrophotometer. From these spectra the film thickness was determined by the interference method.

TABLE 1. Preparation conditions and some physical properties of tin dioxide films, where T_s is the substrate temperature, t is the deposition time, e_0 the film thickness by interference method, e_{RBS} the film thickness from RBS spectra, v_d the deposition rate, and ρ the film resistivity. Sample D is an F-doped SnO_2 film (0.6 wt.% of NH_4F in solution)

Sample	T_s (K)	t (s)	e_0 (nm)	e_{RBS} (nm)	v_d (nm s^{-1})	ρ ($\times 10^{-3} \Omega \text{ cm}$)
A	603	300	220	210	0.73	6.2
B	603	1500	560	620	0.37	3.2
C	643	600	360	340	0.60	14.0
D	573	1500	690	630	0.46	1.8

X-ray diffraction spectra were obtained using a Siemens D5000 X-ray diffractometer at 30 kV and 20 mA. We have used $\text{Cu K}\alpha$ ($\lambda = 1.542 \text{ \AA}$) radiation and the scanning angle 2θ was varied in the range 20-110°. An SiO_2 standard was used to calibrate the diffractometer. The reproducibility and accuracy in 2θ obtained were $\pm 0.0005^\circ$ and $\pm 0.005^\circ$ respectively. The interplanar distance and intensity were

<https://cimav.repositorioinstitucional.mx/jspui/>

obtained using a DIFFRACAT (Siemens) program. The structure, preferential growth directions and mean grain size were evaluated from these spectra.

Transmission electron micrographs and transmission electron diffraction (TED) patterns were obtained in a JEOL-100CX transmission electron microscope. For these studies the films were peeled off the glass substrate by immersion in HF (40%) and then they were floated and rinsed in deionized water; finally they were mounted on a copper grid and ion milling etched for thickness reduction. Different ion milling etching (IME) processes were used: top IME for observing the bottom layers formed nearest the substrate, top-bottom IME for observing intermediate layers, and bottom IME for observing top layers of the films.

Scanning electron micrographs were obtained in a JEOL 5200 scanning electron microscope. For these studies the samples were covered with a very thin layer of gold.

The stoichiometry and film thickness were measured by the well-known He⁺ RBS technique using the 5.5 MeV Van de Graaff accelerator at the Instituto de Fisica, Universidad Nacional Autónoma de México. The He beam energy was fixed at 2 MeV and a solid state detector was used to detect the backscattered He particles at 165 °. The RBS spectra were analysed with a RUMP program, which is a series of FORTRAN subroutines designed [11] for the analysis and simulation of RBS data. It is commercially available from Computer Graphics Service, Lassing, NY.

Results and discussion

Advantages of the new improved method:

The forces that determine the path of droplets in a corona spray system were described in detail by Siefert [3]. In our system, only the gravitational and Stokes forces act on the droplets in the spraying chamber and nozzle. These two forces will reach equilibrium, and the droplets will travel with a constant velocity called the terminal velocity. Calculations of this velocity (for a typical air flow of 250 ml s^{-1}) show that, in the upper section of the nozzle (Fig. 1), the droplets with radii greater than $26 \text{ }\mu\text{m}$ will have a negative terminal velocity, i.e. the droplets are going down, and only the smaller droplets will reach the reaction zone. Figure 2 shows the terminal velocity as a function of the droplet radii, for a mean air velocity of $8 \times 10^{-3} \text{ ms}^{-1}$. In addition, the counterflux spray system provides a laminar flow of the carrier gas into the deposition chamber. With this system the vorticity due to the spray gas was completely eliminated in the nozzle, far away from the deposition chamber.

In the overhead deposition chamber, both the thermophoretic and gravitational forces with the laminar flow geometry used in this system delay the larger droplets (radius, greater than $10 \text{ }\mu\text{m}$), forcing them to take more time to reach the substrate; on the contrary the smaller droplets (below $10 \text{ }\mu\text{m}$) reach the substrate without any important perturbation, as shown by the variation in the terminal velocity of the droplets (Fig. 2). In these conditions the deposition parameters (particularly the substrate temperature) can be adjusted for optimal reaction kinetics for the actual size and distribution of droplets and for a fixed mass flow rate.

The overhead hot-plate has another advantage, namely the suppression of vorticity due to the convection flow of the hot gases as in the conventional bottom

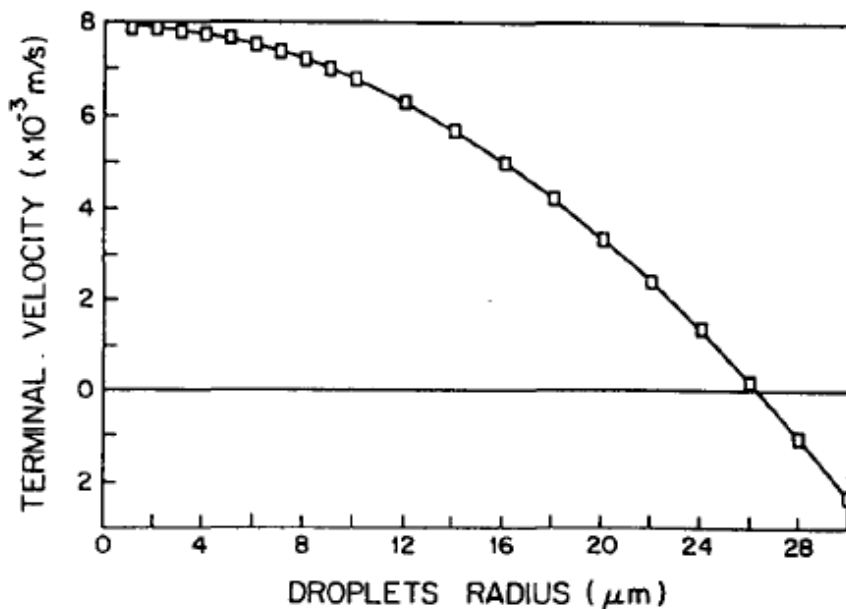


Fig. 2. Terminal velocity of droplets into the nozzle, as a function of droplet radius. The mean air velocity is $8 \times 10^{-3} \text{ m s}^{-1}$.

hot-plate. Moreover, the lateral screening LS and the bottom plate BP from a nearly closed deposition chamber, free of ambient contamination. The only limitation of this type of deposition chamber is the possible contamination with the exhaust gases formed in the pyrohydrolytic reaction; this can be avoided by ensuring adequate ventilation and optimum deposition parameters, such as substrate temperature, carrier gas flow, mist flow and concentration of source material.

Structure analysis:

Films obtained at substrate temperatures below 523 K were amorphous; at higher temperatures they were polycrystalline and showed a preferential growth direction, which was film thickness dependent. Figure 3 shows the X-ray diffraction

spectra for films A, B, C and D. For depositions at 603 K, sample A did not show any marked preferential growth direction, but sample B clearly showed a (211) preferential direction, i.e. grains develop preferentially with (211) planes parallel to the substrate. In addition, no variation in growth direction was observed as the substrate temperature was varied between 603 and 643 K (if we compare films of almost the same thickness), as can be seen in the spectrum of film C obtained at 643 K. Sample D also shows a (211) preferential growth direction. Additionally in Table 2 the interplanar distance d_x and intensity I_{hkl} of several reflections from X-ray diffraction spectra of the same films are compared with the data obtained on a powder sample by the Joint Committee for Powder Diffraction Standards (JCPDS) [12].

The mean grain size of the films was calculated using Scherrer's formula [13], assuming that microstrains are negligible, as evidenced by the TEM-SEM analysis. The mean grain size is defined as the mean dimension of the crystallite perpendicular to the diffracting plane. According to this definition, the constant factor in Scherrer's formula is taken as 0.9 [13]. An SnO₂ powder sample (greater than 99.5% purity) was used as a standard for determination of the instrumental peak

TABLE 2. Comparison of the calculated interplanar distance d_x and peak intensity I_{hkl} from X-ray diffraction spectra of films A, B, C, D and Joint Committee of Powder Diffraction Standards powder sample (the interplanar distance d_c calculated from the ring radii of the transmission electron diffraction patterns for films A, B and C is also shown)

(hkl)	JCPDS sample		Sample A			Sample B			Sample C			Sample D	
	d_{pw} (Å)	I_{pw} (%)	d_c (Å)	d_x (Å)	I_{hkl} (%)	d_c (Å)	d_x (Å)	I_{hkl} (%)	d_c (Å)	d_x (Å)	I_{hkl} (%)	d_x (Å)	I_{hkl} (%)
(110)	3.351	100	3.35	3.37	100	3.37	3.37	86	3.35	3.35	100	3.37	100
(101)	2.644	80	2.65	2.65	33	2.66	2.65	89	2.66	2.65	39	2.66	36
(200)	2.369	25	2.38	2.38	35	2.35	2.38	57		2.37	32	2.38	81
(111)	2.309	6							2.33				
(210)	2.120	2	2.11			2.13			2.13				
(211)	1.765	65	1.76	1.77	33	1.77	1.77	100	1.77	1.77	36	1.77	90
(220)	1.675	18		1.68	15	1.68	1.68	13	1.68	1.68	14	1.68	19
(002)	1.593	8				1.59			1.58				
(310)	1.498	14		1.51	15	1.50	1.50	21	1.50	1.50	16	1.50	28
(301)	1.415	16		1.42	19	1.43	1.42	42	1.43	1.42	16	1.42	45

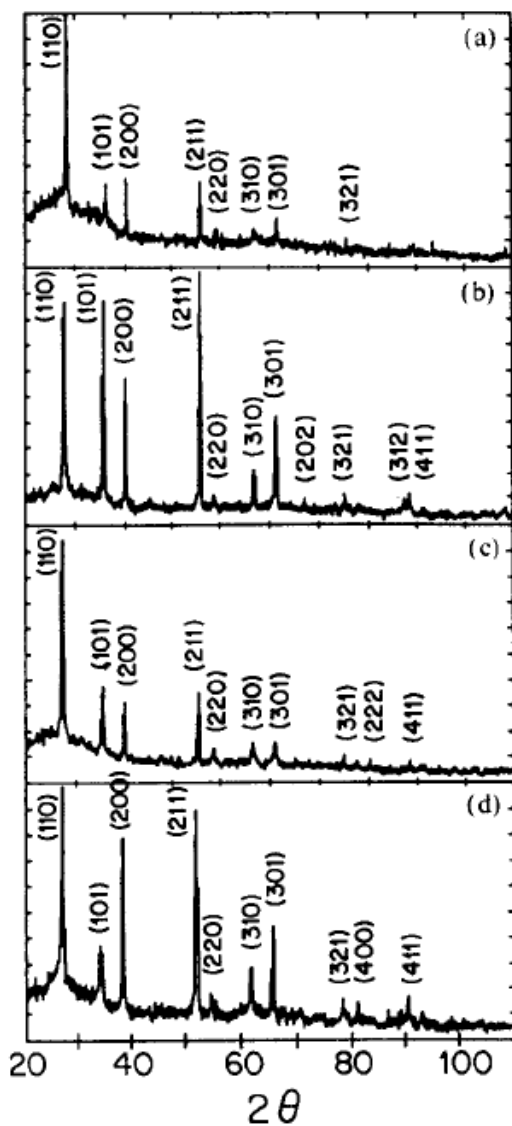


Fig. 3. X-ray diffraction spectra: (a) sample A, $T_s = 603$ K, $e = 220$ nm; (b) sample B, $T_s = 603$ K, $e = 560$ nm; (c) sample C, $T_s = 643$ K, $e = 360$ nm; (d) sample D, $T_s = 573$ K, $e = 690$ nm, doped with F (0.6 wt.% in solution).

broadening. This broadening was taken as the halfmaximum peak breadth of each reflection in the standard spectrum. Figure 4 shows the grain size calculated for reflections (110), (101), (200) and (211) from X-ray diffraction spectra. It is seen that there is a slight increase in grain size as the film thickness varies between 220 and 560

nm (samples A and B), for (110), (101) and (211) reflections, and an important increase for the (200) reflection. Also a slight decrease in grain size is observed when the substrate temperature varies between 603 and 643 K (samples A and C), for (101), (200) and (211) reflections; however, for (110) a slight increase is observed. For the doped sample D, the grain sizes are smaller than in all other samples, for all reflections.

Table 3 shows a comparison of grain sizes calculated from X-ray diffraction spectra, with those obtained from transmission electron micrographs and with surface grain sizes observed in scanning electron micrographs. There is an observed tendency for the grain sizes determined by X-ray diffraction and TEM to agree, i.e. a decrease with increased substrate temperature and an increase with increased film thickness. Nevertheless the X-ray values are lower than the TEM values, as expected [7]. The surface grain sizes obtained from scanning electron micrographs are larger than both X-ray and TEM values. This discrepancy may be due to the non-uniformity of the film in which the largest grains are on the upper exposed surface.

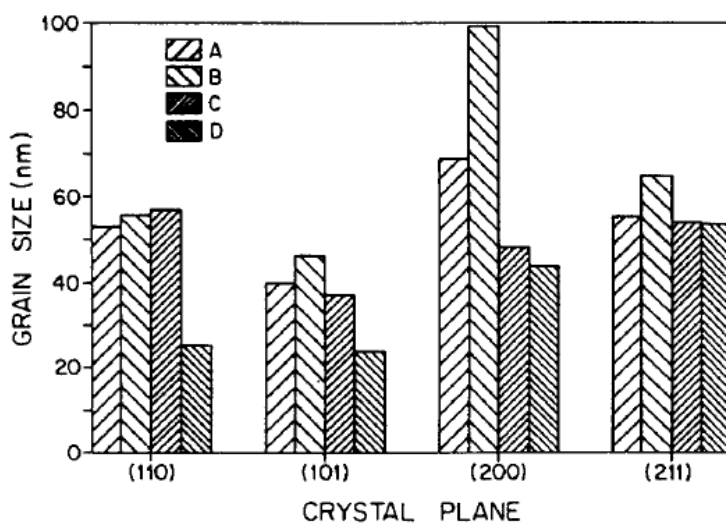


Fig. 4. Grain size for (110), (101), (200) and (211) reflections from X-ray diffraction spectra of samples A, B, C and D.

Figure 5 shows micrographs of different layers of a tin dioxide film, obtained by different IME treatments of the same film. Figure 5(a) shows a bright-field image of a sample in which top IME was realized, therefore showing the first layers grown just over the substrate. The layers show an amorphous phase (labelled A), which had been in contact with the glass substrate. On top of and within this amorphous layer there are many small crystallites of SnO₂ (labelled X), almost circularly shaped, with diameters in the approximate range 3- 14 nm, also reported by Fujimoto et al. [8]. In other zones of the same figure, large crystallites (labelled L) grown on the small crystallites can be seen. The inset shows the TED, in which the diffuse ring observed between the (110) and (101) spot rings confirms the existence of the amorphous phase. Dark-field images (Fig. 6) obtained with the objective aperture in this zone of the diffraction pattern also confirm the existence of the small crystallites embedded in the amorphous matrix.

Figure 5(b) shows a bright-field image of a sample in which top-bottom IME was performed, therefore showing an intermediate layer between the top surface of the film and the bottom layer. In this intermediate layer we clearly see a closely packed structure of crystallites with many defects, twin boundaries and dislocations; their grain sizes range between 25 and 120 nm. A careful analysis of this micrograph shows, in a few zones, lattice fringes spaced about 0.83 nm, which should correspond to small crystallites of Sn₂O₃ or Sn₃O₄ of about 25 nm size. The TED pattern is seen in the inset of the same figure. No more diffuse rings are found; only many rings with spots are seen.

Figure 5(c) shows a bright-field image of a sample in which bottom IME was performed. In this micrograph, one can see the crystallites of the top layer; one can also

note a different morphology with fewer defects. Some crystals of Stoneham or Zinnwald type can also be identified (labelled S and Z respectively), which are two different morphologies observed in natural cassiterite crystals [14]. The grain size, ranging between 60 and 170 nm, is larger than in the intermediate layers. The grain boundaries

TABLE 3. Comparison between grain size calculated from X-ray diffraction spectra, with that obtained from transmission electron micrographs of films A, B and C and surface grain size observed in scanning electron micrographs

	Grain size (nm)			
	Sample A	Sample B	Sample C	Sample D
X-ray spectra	40–70	45–100	35–60	25–55
Transmission electron micrograph	60–170	140–300	30–120	—
Surface by SEM	40–200	80–400	80–400	20–80

are thin, and also many small clusters, which should be nucleation centres, can be observed in the faces of some crystals (labelled N). The cluster size varied between 3 and 7 nm. The insert shows a TED pattern similar to that of the intermediate layer.

Table 2 also shows the interplanar distance d_e calculated from the ring radii of the TED patterns for films A, B and C, and their corresponding (hkl) Miller indices.

Film growth:

The deposition rate was obtained from measurements of the film thickness, determined from optical transmission data and deposition time. Figure 7 shows a logarithmic plot of deposition rate vs. $1000/T$ s, where T s is the substrate temperature. The full lines are least-squares fits in the two different regimes of deposition rate observed as a function of substrate temperature: at high temperatures (above 633 K), a temperature-independent region, in which the growth rate is mass transport controlled, by diffusion of reactants to the substrate surface or by diffusion of product gases out of the substrate surface [15]; at lower temperatures (below 633 K), an activated region with an activation energy of 8.5×10^{-20} J (0.53 eV), in which the deposition rate is

limited by the reaction kinetics, i.e. by a process occurring at or near the substrate surface [15]. This behavior has been reported previously by several workers [16-18].

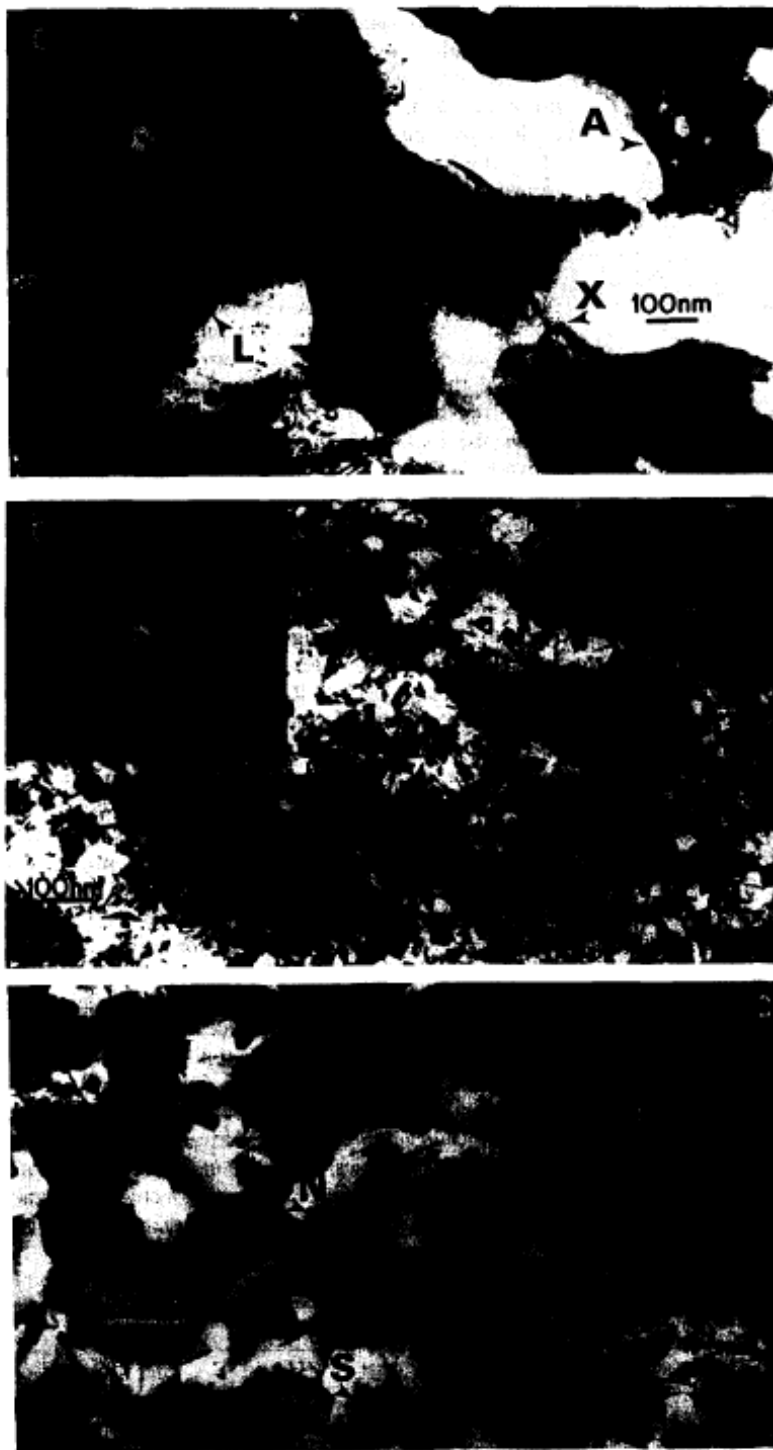


Fig. 5. Transmission electron micrographs of different layers of a typical tin dioxide film, and insets showing TED patterns: (a) bottom layers (first formed), showing the amorphous phase (labelled A), small crystallites (labelled X) and large crystallites (labelled L); (b) intermediate layer; (c) top layer, showing some crystals of Stoneham (labelled S) and Zinnwald (labelled Z) type.

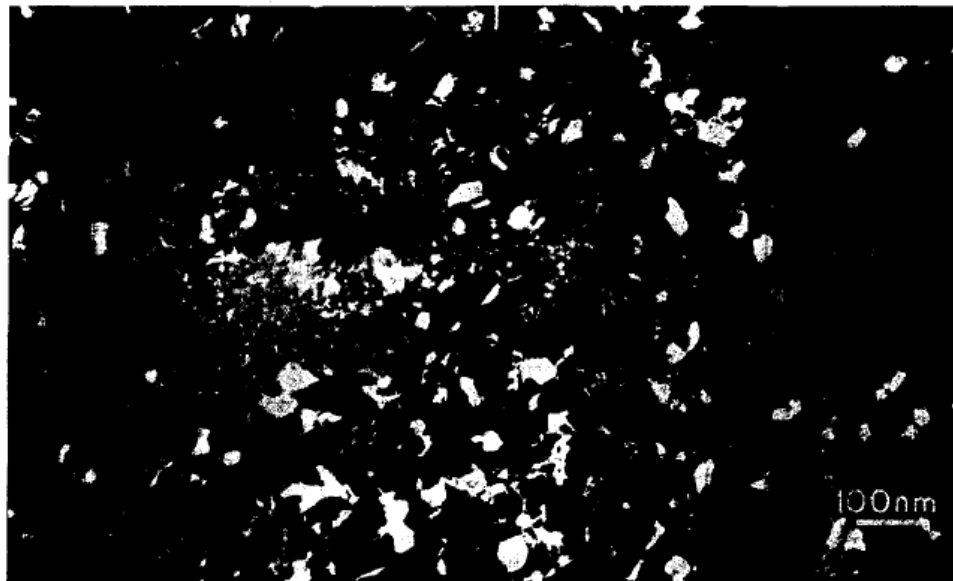


Fig. 6. Dark-field image, showing the amorphous phase and small crystallites.

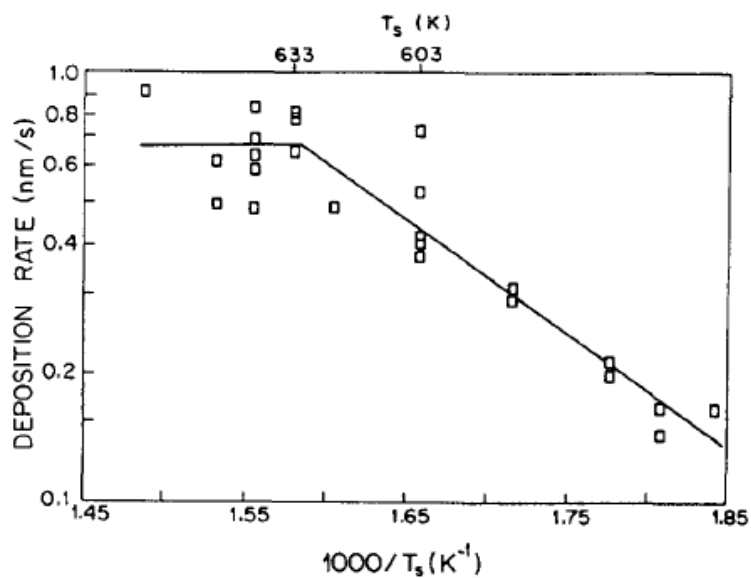


Fig. 7. Logarithmic plot of the deposition rate vs. $1000/T_s$, T_s being the substrate temperature.

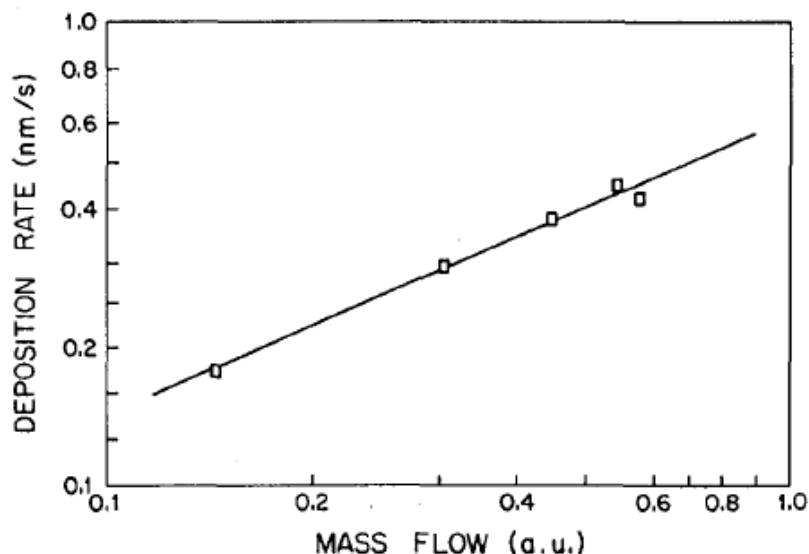


Fig. 8. log-log plot of deposition rate vs. mass flow rate (a.u., arbitrary units).

Figure 8 shows a log-log plot of deposition rate vs. mass flow rate, for films obtained at 603 K. The mass flow was proportional to the solution concentration multiplied by the average mist flow rate. We have varied the solution concentration between 0.05 and 0.5 M and measured the initial and final volumes of solution to calculate the average mist flow rate. The plot in Fig. 8 is a straight line over almost the whole interval analysed. Its slope, calculated by a linear leastsquares fit, is approximately 0.64, not very different from the 0.5 power dependence in the case of CVD [19]. Then we have the following power dependence of deposition rate to the mass flow:

$$v_d \propto m^{0.64}$$

where m is the average mass flow rate. This dependence indicates that, for the interval analysed, the growth is mass transport controlled.

Thus for a substrate temperature of 603 K the mass flow rate limit between the mass transport region and reaction kinetics region will be about 3 mg s^{-1} of source compound ($\text{SnCl}_4 \cdot 5\text{H}_2\text{O}$); below this limit the process is mass transport controlled and, above this limit it is controlled by the reaction kinetics of the process. This mass flow rate corresponds approximately to a mist flow rate of $3 \times 10^{-2} \text{ ml s}^{-1}$ of a 0.3 M solution.

Figure 9 shows the thickness dependence of deposition rate for two substrate temperatures (all other deposition parameters are fixed). A decrease in the growth rate is observed as the film thickness increases. This thickness dependence of the growth rate suggests that it could be explained by a mechanism similar to that of inhibited particle growth [20], already reported for the growth of metal particles supported on metal oxide substrates. The growth rate will be thickness dependent because repeated nucleation events on the crystallite faces are necessary for later stages of growth. This result is consistent with our grain size calculation and the observed transmission electron micrographs.

In the case of In_2O_3 films, Muranaka et al. [9] have observed the same amorphous phase and embedded crystallites for films 2.5 nm thick, and a closely packed microstructure for films 30 nm thick. They concluded that an amorphous-to-crystalline transformation of the film occurs as the film thickness increases, but our results indicate that, in tin dioxide films, the amorphous phase and small crystallites are still there, even for films of thickness as large as 600 nm, and they are not seen in transmission electron micrographs because of their poor contrast. Thus Fig. 5 suggests that the films start to grow amorphous, then the film growth continues with nucleation of many small crystallites, and finally some of them continue to grow until a closely packed

microstructure of crystallites is formed. These growth steps should be temperature dependent, since the amorphous-to-polycrystalline transition temperature was determined to be around 523 K, in agreement with other work [21].

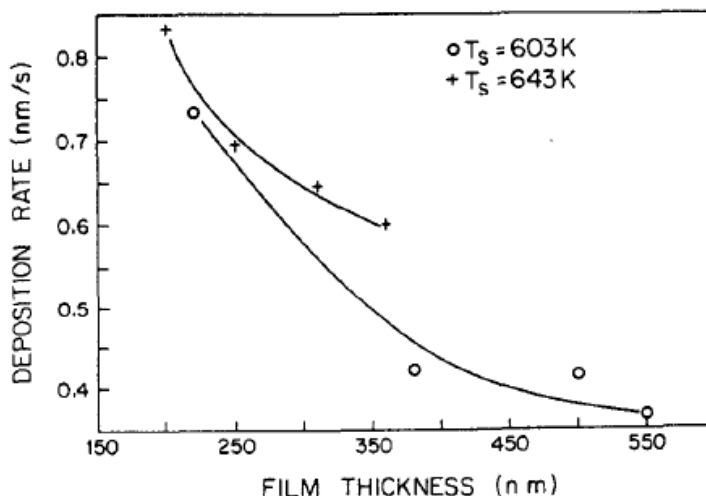


Fig. 9. Deposition rate vs. film thickness: \circ , $T_s = 603\text{ K}$; $+$, $T_s = 643\text{ K}$.

Film composition:

Figure 10 shows a typical He⁺ RBS spectrum of tin dioxide films (full circles) and their computer simulation (full curve) using the RUMP program. From this simulation the film thickness was found by means of the energy shift of the Sn peak [22] and it is tabulated in Table 1 (eRas); there is good agreement with the calculated optical thickness within 10%. For undoped films the film stoichiometry was close to the SnO₂ phase and for doped films a slight oxygen diminution was determined. The contamination by Cl and Na was less than 1%, as determined by RUMP simulation. Another interesting result is the slight reduction in Sn and O concentration in the outer portion of the tin dioxide film, which is probably due to a density variation in the film near

the surface, since the Sn-to-O ratios are almost the same. This behaviour is in agreement with the Auger depth profile reported previously by Kim et al. [23].

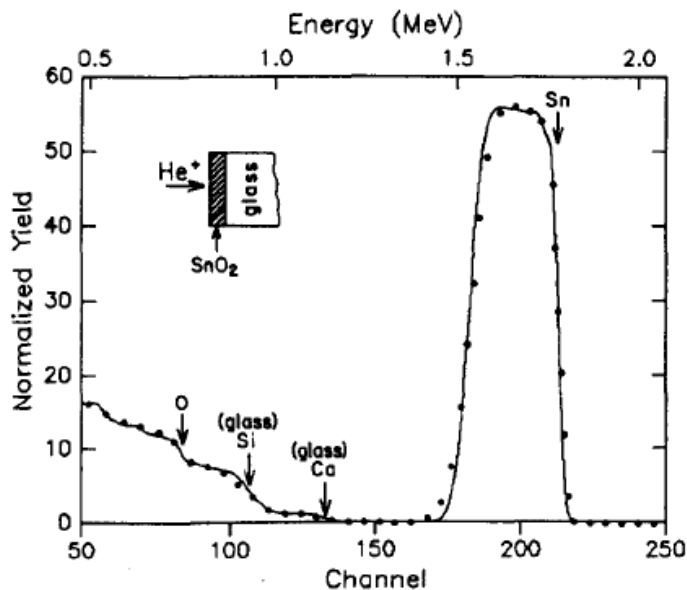


Fig. 10. Typical RBS spectrum (●) of a tin dioxide and RUMP simulation (—).

Surface roughness:

The surface roughness of the films was studied by SEM. Figure 11 shows SEM micrographs of films A, B and C. Different surface roughnesses were observed for these films. Figure 11(a) shows that the surface of film A is very smooth; however Figs. 11(b) and 11(c) show that the surfaces of films B and C show many cavities, ranging between 90 and 420 nm. This surface roughness could be responsible for the large decrease in optical transmission obtained in the visible region (Fig. 12), for films B and C, since surface roughness causes multiple reflections of incident light [21]. This is reinforced by the fact that no significant Cl contamination was detected.



Fig. 11. Scanning electron micrographs of films A, B and C showing surface roughness: (a) sample A; (b) sample B; (c) sample C.

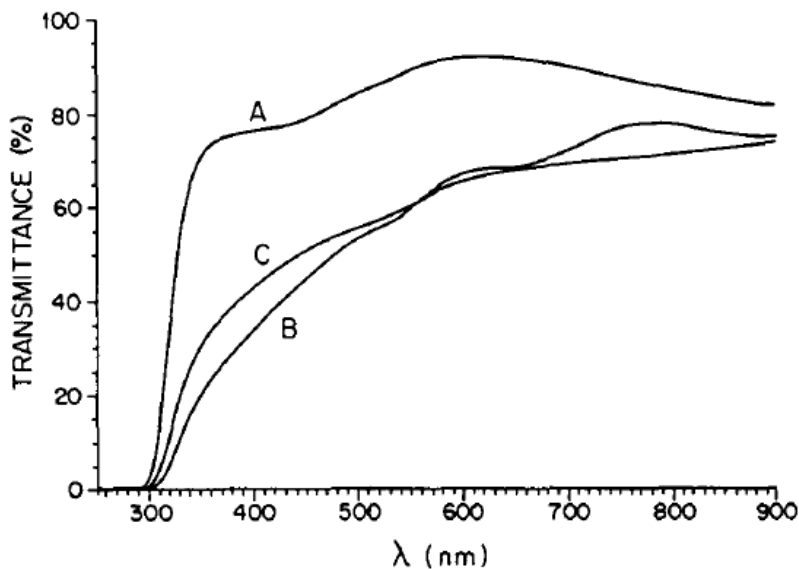


Fig. 12. Optical transmittance spectra of films A, B and C.

Conclusion

The spray pyrohydrolysis system used in this work has the following advantages: good size selectivity of the droplets that arrive close to the substrate, a suppression of vorticity due to the spray gas in the spraying chamber, and reduced convection flow of the hot gases in the deposition chamber. The decrease in the growth rate as the film thickness increases suggests that it could be explained by a mechanism similar to that of an inhibited particle growth, this proposition being consistent with TEM observation of the film microstructures. The observation of different layers of film microstructure by TEM suggests that the films start to grow amorphous, then film growth continues with nucleation of many small crystallites, and finally some grow until a closely packed microstructure is formed. There is not an amorphous-to-crystalline transition during film growth as reported for In_2O_3 . No significant contamination by Cl and Na was determined by RBS analysis (less than 1%). Therefore the decrease in optical transmittance in the

visible region could be due to the surface roughness of the films. We can also conclude that the film thickness is an important parameter that must be present when comparing physical properties of thin films, i.e. comparison must be done for a constant film thickness.

Acknowledgments

The authors would like to thank Dr. M. José-Yacamán and Dr. W. Estrada for very useful discussions.

They wish to express their appreciation to R. Hernández, J. C. Pineda, E. P. Zavala, F. Fernfindez R., J. Cafietas, A. Morales and E. Hernández for assistance with the experimental work and to R. Bashi, V. Quinde and J. Farffin for construction of the experimental set-up. Also they are grateful to the Optical Properties Laboratory, Solid State Department, Instituto de Fisica, Universidad Nacional Autónoma de México, for optical measurements. Also one of us (MMY) is indebted to DGAPA, Universidad Nacional Autónoma de México, and Consejo Nacional de Ciencia y Tecnología de México for a post-doctoral fellowship. This work was partially supported by a grant from Third World Academy of Science (Trieste Italy), Instituto General de Investigación, Universidad Nacional de Ingeniería (Lima, Peru) and Dirección General de Asuntos del Personal Académico, Universidad Nacional Autónoma de México (Mexico).

References

- 1 J. Kane, H. P. Scheweizer and W. Kern, J. Electrochem. Soc., 123 (1976) 270.

<https://cimav.repositorioinstitucional.mx/jspui/>

2 G. Blandenet, M. Court and Y. Lagarde, *Thin Solid Films*, 77

(1981) 81.

3 W. Siefert, *Thin Solid Films*, 121 (1984) 267.

4 H. W. Lehmann and R. Widmer, *Thin Solid Films*, 27(1975) 359.

5 W. Spence, *J. Appl. Phys.*, 38 (1967) 3767.

6 B. Gottlieb, R. Koropecski, R. Arce, R. Crisalle and J. Ferr6n.

Thin Solid Films, 199 (1991) 13.

S. Muranaka, Y. Bando and T. Takada, *Thin Solid Films*, 86

(1981) II.

7 H. Haitjema and J. J. Ph. Elich, *Thin Solid Films*, 205 (1991)

93.

8 M. Fujimoto, T. Urano, S. Murai and Y. Nishi, *Jpn. J. Appl.*

Phys., 28 (1989) 2587.

9 S. Muranaka, Y. Bando and T. Takada, *Thin Solid Films*, 151

(1987) 355.

10 G. Haacke, *J. Appl. Phys.*, 47 (1976) 4086.

11 L. R. Doolittle, *Nucl. Instrum. Methods B*, 15 (1986)227.

12 Joint Committee on Powder Diffraction Standards, *Powder*

<https://cimav.repositorioinstitucional.mx/jspui/>

Diffraction File, International Center for Diffraction Data,

Swarthmore, PA, 1988, Card 21-1250.

13 E. F. Kaelble, (ed.), Handbook of X-rays, Part 2, McGraw-Hill,

New York, 1967, Chapter 17.

14 Dana's System of Mineralogy, Vol. 1, 7th edn., Wiley, New York,

1944, pp. 574-581.

15 W. A. Bryant, J. Mater. Sei., 12 (1977) 1285.

16 J. Sanz Maudez and T. Rodriguez, Thin Solid Films, 69 (1980)

183.

17 F. Caillaud, A. Smith and J. F. Baumard, Thin Solid Films, 208

(1992) 4.

18 V. Vasu and A. Subrahmanyam, Thin Solid Films, 189 (1990)

217.

19 H. Schlichting, Boundary Layer Theory, McGraw-Hill, New York,

1960, Chapter 7.

20 P. Wynblatt and N. A. Gjostein, Acta Metall., 24 (1976) 1165.

21 M. Fantini and I. Torriani, Thin Solid Films, 138 (1986) 255.

22 W. K. Chu, J. W. Mayer and M. A. Nicolet, Backscattering

<https://cimav.repositorioinstitucional.mx/jspui/>

Spectrometo,, Academic Press, New York, 1978, Chapter 5.

23 K. Kim, T. G. Finstad, W. K. Chu, X. B. Cox and R. W. Linton,

Sol. Cells, 13 (1984-1985) 301.